JOURNAL OF COMPUTATIONAL PHYSICS **125,** 378–394 (1996)
ARTICLE NO. 0100

A Comparative Study of Characteristic-Based Algorithms for the Maxwell Equations

J. S. SHANG AND ROBERT M. FITHEN

Flight Dynamics Directorate, U.S. Air Force Wright Laboratory, Wright–Patterson Air Force Base, Ohio 45433

Received July 5, 1994; revised July 31, 1995

Characteristic-based finite-difference and finite-volume schemes have been developed for solving the three-dimensional Maxwell equations in the time domain. A detailed eigenvector analysis for the Maxwell equations in a general curvilinear coordinate has also been completed to provide a basic framework for future finite-difference schemes. Although the basic concepts of the two algorithms are identical, the detailed formulations are vastly different for achieving split flux vectors according to the sign of the eigenvalues. A comparative study of these algorithms applied to an oscillating electric dipole is carried out to assess their relative merit for further development. In spherical coordinates, second-order windward numerical simulations of the radiating phenomenon are closely comparable in terms of accuracy and efficiency. These methods also demonstrate an ability to suppress reflected waves from the truncated boundary by a simple compatibility condition.

NOMENCLATURE

$\overline{B}$	Magnetic flux density
$\overline{D}$	Electric displacement
$\overline{E}$	Electric field intensity
F	Flux vector component
$\overline{H}$	Magnetic field intensity
i, j, k	Index of discretization
J	Electric current density
n	Temporal index of solution
S	Similarity transformation matrix
t	Time
x, y, z	Cartesian coordinates
r, θ, ϕ	Spherical coordinates
U	Dependent variables
V	Jacobian of coordinate transformation
ε	Electric permittivity
μ	Magnetic permeability
λ	Eigenvalue
ξ, η, ζ	Transformed coordinates

Superscript

$+$	Denotes association with positive eigenvalue
$-$	Denotes association with negative eigenvalue
-1	Denotes matrix inverse operation

I. INTRODUCTION

The Maxwell equations in the time domain constitute a hyperbolic partial differential system which is a pure initial-value problem. Simulations of the electromagnetic phenomenon by solving the basic equations on a computer system are always limited by the memory size. This constraint compels the calculations to be conducted in a truncated computational domain, which unavoidably introduces an artificial boundary to an initial-value problem. This artifact has been known to induce spurious wave reflections from the truncated boundary and to incur sizable numerical errors [1–3]. In oder to eliminate or to alleviate the wave reflection from numerical boundaries, either a compatibility condition derived from the characteristic theory [4, 5], or an absorbing boundary condition [6–8] is frequently implemented at the farfield boundary. The characteristic based concept of compatibility is preferred over the others, because the numerical procedure also enforces the directional propagation of information for wave motion. In essence, the characteristic formulation honors the physical zone of dependence.

A body-oriented, curvilinear coordinate system can greatly facilitate the computation of an electromagnetic field around a complex scatterer. The time dependent Maxwell equations can be cast in a general curvilinear coordinate system by a coordinate transformation from the Cartesian frame of reference. In the transformed space, the metrics of coordinate transformation are position dependent and the system of equations will have variable coefficients. As a direct consequence, the characteristic-based formulation is no longer reducible to the Riemann problem [5, 9, 10]. The rather complex eigenvalue and eigenvector structure of the Maxwell equations has also inhibited a systematic discretization effort. For this reason, some finite-difference schemes, when applied to a non-

0021-9991/96 $18.00

rectangular scatterer, rely on an interpolation procedure to satisfy the boundary conditions [1].

A viable alternative to this approach is to employ the finite-volume approximation, in which a detailed eigenvector analysis in the transformed domain is unnecessary [2, 10]. On a general curvilinear frame, the finite-volume formulation requires only a locally orthogonal coordinate system on control surfaces to balance the flux vectors across each cell. The Cartesian frame is the most elementary orthogonal set, which is also the present coordinates of reference. The eigenvalues and eigenvectors of the locally orthogonal coordinates are nearly identical to those of the Cartesian frame [10], so an elaborate eigenvalue and eigenvector analysis is completely circumvented. For this reason, the development of characteristic-based finite-volume schemes preceded that of finite-difference methods [2, 10]. For all finite-volume approximations, the required metric information is generated exclusively from vertexes and edges of the elementary cell. At the cell surfaces, the reconstruction of the flux vector involves either an interpolation or an extrapolation procedure to achieve higher order accuracy [10–14]. The numerical accuracy of a finite-volume scheme is therefore dictated by the metrics and the reconstructed flux calculations.

The finite-volume scheme is generally devoid of discretization error due to a non-conservative formulation [15]. However, for computational electromagnetics, there is no overly significant advantage of a strong conservative formulation. Except for the relationship between electric charge and current density, Maxwell equations do not explicitly describe a conservative law [16–18]. For most problems, sources of electromagnetic fields are prescribed and this conservation law is automatically satisfied [16]. The finite-volume scheme also has an inherent emphasis in describing the global behavior of a simulated field. Therefore, this scheme has a greater capacity for reproducing rapid variations induced by a geometric singularity than the finite-difference scheme. On the other hand, the issue of numerical accuracy of finite-volume algorithms becomes more acute when implemented on a highly stretched and non-rectangular cell structure. The empirical rule of thumb is that the numerical result will be degraded slightly, even though the formal order of accuracy is reduced [14]. Under this circumstance, the quantification of numerical accuracy is uncertain but needs a concise delineation for future applications.

The present study attempts to compare directly two characterisic-based finite-difference and finite-volume algorithms for solving the Maxwell equations in the time domain. Since a finite-volume flux differencing numerical procedure has been implemented previously [2], only the finite-difference flux vector splitting algorithm [19] is implemented for the time-dependent, three-dimensional Maxwell equations. The prerequisite of this development is to conduct detailed eigenvalue and eigenvector analyses for the time-dependent Maxwell equations in each individual coordinate of the transformed space. The equations in flux vector form are split according to the sign of the eigenvalues and solved by a second-order accurate upwind difference technique. The rest of the present efforts are devoted to examining the relative accuracy and aliasing errors in simulating a time dependent electromagnetic phenomenon. The numerical results will be compared with theory for wave propagation in a rectangular wave guide and from an oscillating electric dipole [17, 18]. Computations have been simulated using the Cartesian frame and a spherical coordinate system, respectively.

II. GOVERNING EQUATIONS

The time-dependent Maxwell equations for an electromagnetic field can be given as [16–18]

$$\frac{\partial \overline{B}}{\partial t} + \nabla \times \overline{E} = 0 \tag{1}$$

$$\frac{\partial \overline{D}}{\partial t} - \nabla \times \overline{H} = -\overline{J} \tag{2}$$

$$\nabla \cdot \overline{B} = 0, \quad \overline{B} = \mu \overline{H} \tag{3}$$

$$\nabla \cdot \overline{D} = 0, \quad \overline{D} = \varepsilon \overline{E}. \tag{4}$$

In a Cartesian frame, the system of equations written in flux vector form becomes [4, 5, 10]

$$\frac{\partial U}{\partial t} + \frac{\partial F_x}{\partial x} + \frac{\partial F_y}{\partial y} + \frac{\partial F_z}{\partial z} = -J \tag{5}$$

The one-dimensional, characteristic-based formulation is easily constructed from the eigenvalue and eigenvector analysis. The essential diagonalization process is simply to construct a non-singular similarity matrix and its left-hand inverse from the eigenvectors in each spatial dimension [4, 5, 9]. In a Cartesian frame, the Maxwell equations for an isotropic and homogeneous medium have constant coefficients. Thus, all eigenvalues and eigenvectors are invariant with respect to independent variables. The resultant split one-dimensional equations for the three-dimensional problem are completely decoupled and consist of 12 scalar Riemann equations [4, 5]. In this formulation, accurate simulation of electromagnetic phenomenon is restricted to fields that can be described by rectilinear coordinates.

The time-dependent Maxwell equations in general curvilinear coordinates can be derived by a coordinate transformation. The most general coordinate transformation in-

cludes a one-to-one relationship between two sets of temporal and spatial independent variables. However, for most practical applications, a coordinate transformation involving spatial variables is sufficient:

$$\begin{aligned}\xi &= \xi(x, y, z)\\ \eta &= \eta(x, y, z)\\ \zeta &= \zeta(x, y, z).\end{aligned} \tag{6}$$

The strong conservation from is obtained by dividing the chain-rule-differentiated equations by the Jacobian of coordinate transformation and by invoking metric identities [10]. The strong conservative form of the governing equations is

$$\frac{\partial U}{\partial t} + \frac{\partial F_\xi}{\partial \xi} + \frac{\partial F_\eta}{\partial \eta} + \frac{\partial F_\zeta}{\partial \zeta} = -J, \tag{7}$$

where the transformed dependent variables remained unaltered but are now scaled by the Jacobian of coordinate transformation:

$$U = U\left(\frac{B_x}{V}, \frac{B_y}{V}, \frac{B_z}{V}, \frac{D_x}{V}, \frac{D_y}{V}, \frac{D_z}{V}\right). \tag{8}$$

The flux vector components F_ξ, F_η, and F_ζ in Eq. (7) are products of the metrics of coordinate transformation and the Cartesian components, $F_\xi = \xi_x F_x + \xi_y F_y + \xi_z F_z$, $F_\eta = \eta_x F_x + \eta_y F_y + \eta_z F_z$, and $F_\zeta = \zeta_x F_x + \zeta_y F_y + \zeta_z F_z$. The specific expressions are

$$F_\xi = \begin{bmatrix} 0 & 0 & 0 & 0 & -\frac{\xi_z}{\varepsilon V} & \frac{\xi_y}{\varepsilon V} \\ 0 & 0 & 0 & \frac{\xi_z}{\varepsilon V} & 0 & -\frac{\xi_x}{\varepsilon V} \\ 0 & 0 & 0 & -\frac{\xi_y}{\varepsilon V} & \frac{\xi_x}{\varepsilon V} & 0 \\ 0 & \frac{\xi_x}{V\mu} & -\frac{\xi_y}{V\mu} & 0 & 0 & 0 \\ -\frac{\xi_z}{V\mu} & 0 & \frac{\xi_x}{V\mu} & 0 & 0 & 0 \\ \frac{\xi_y}{V\mu} & -\frac{\xi_x}{V\mu} & 0 & 0 & 0 & 0 \end{bmatrix} \begin{Bmatrix} B_x \\ B_y \\ B_z \\ D_x \\ D_y \\ D_z \end{Bmatrix} \tag{9}$$

$$F_\eta = \begin{bmatrix} 0 & 0 & 0 & 0 & -\frac{\eta_z}{\varepsilon V} & \frac{\eta_y}{\varepsilon V} \\ 0 & 0 & 0 & \frac{\eta_z}{\varepsilon V} & 0 & -\frac{\eta_x}{\varepsilon V} \\ 0 & 0 & 0 & -\frac{\eta_y}{\varepsilon V} & \frac{\eta_x}{\varepsilon V} & 0 \\ 0 & \frac{\eta_x}{V\mu} & -\frac{\eta_y}{V\mu} & 0 & 0 & 0 \\ -\frac{\eta_z}{V\mu} & 0 & \frac{\eta_x}{V\mu} & 0 & 0 & 0 \\ \frac{\eta_y}{V\mu} & -\frac{\eta_x}{V\mu} & 0 & 0 & 0 & 0 \end{bmatrix} \begin{Bmatrix} B_x \\ B_y \\ B_z \\ D_x \\ D_y \\ D_z \end{Bmatrix} \tag{10}$$

$$F_\zeta = \begin{bmatrix} 0 & 0 & 0 & 0 & -\frac{\zeta_z}{\varepsilon V} & \frac{\zeta_y}{\varepsilon V} \\ 0 & 0 & 0 & \frac{\zeta_z}{\varepsilon V} & 0 & -\frac{\zeta_x}{\varepsilon V} \\ 0 & 0 & 0 & -\frac{\zeta_y}{\varepsilon V} & \frac{\zeta_x}{\varepsilon V} & 0 \\ 0 & \frac{\zeta_x}{V\mu} & -\frac{\zeta_y}{V\mu} & 0 & 0 & 0 \\ -\frac{\zeta_z}{V\mu} & 0 & \frac{\zeta_x}{V\mu} & 0 & 0 & 0 \\ \frac{\zeta_y}{V\mu} & -\frac{\zeta_x}{V\mu} & 0 & 0 & 0 & 0 \end{bmatrix} \begin{Bmatrix} B_x \\ B_y \\ B_z \\ D_x \\ D_y \\ D_z \end{Bmatrix}, \tag{11}$$

where V is the Jacobian of coordinate transformation. In the finite-volume formulation, it is also the reciprocal of the local cell volume. The mapping between the physical and the transformed space is unique, if the Jacobian has non-zero value within the computational domain:

$$V = \det \begin{bmatrix} \xi_x & \eta_x & \zeta_x \\ \xi_y & \eta_y & \zeta_y \\ \xi_z & \eta_z & \zeta_z \end{bmatrix} \tag{12}$$

and ξ_x, η_x, ζ_x, etc., are the metrics of coordinate transformation.

III. EIGENVALUES AND EIGENVECTORS

In each temporal and spatial plane t–ξ, t–η, and t–ζ, the eigenvalues are easily found by solving the six-degree

characteristic equation associated with the coefficient matrices,

$$\lambda_\xi = \left\{ -\frac{\alpha}{V\sqrt{\varepsilon\mu}}, -\frac{\alpha}{V\sqrt{\varepsilon\mu}}, \frac{\alpha}{V\sqrt{\varepsilon\mu}}, \frac{\alpha}{V\sqrt{\varepsilon\mu}}, 0, 0 \right\} \tag{13}$$

$$\lambda_\eta = \left\{ -\frac{\beta}{V\sqrt{\varepsilon\mu}}, -\frac{\beta}{V\sqrt{\varepsilon\mu}}, \frac{\beta}{V\sqrt{\varepsilon\mu}}, \frac{\beta}{V\sqrt{\varepsilon\mu}}, 0, 0 \right\} \tag{14}$$

$$\lambda_\zeta = \left\{ -\frac{\gamma}{V\sqrt{\varepsilon\mu}}, -\frac{\gamma}{V\sqrt{\varepsilon\mu}}, \frac{\gamma}{V\sqrt{\varepsilon\mu}}, \frac{\gamma}{V\sqrt{\varepsilon\mu}}, 0, 0 \right\}, \tag{15}$$

where

$$\alpha = \sqrt{\xi_z^2 + \xi_y^2 + \xi_x^2}$$
$$\beta = \sqrt{\eta_z^2 + \eta_y^2 + \eta_x^2}$$
$$\gamma = \sqrt{\zeta_z^2 + \zeta_y^2 + \zeta_x^2}.$$

One recognizes that the eigenvalues contain multiplicities, and hence the eigenvectors are not unique [5, 9,10]. Nevertheless, linearly independent eigenvectors still have been found by reducing the coefficient matrices to the Jordan normal form. For consistency, the eigenvectors are selected in such a fashion that similar matrices of diagonalization degenerate to the same form as in the Cartesian frame. From the eigenvector analysis, the similar matrices of diagonalization in each time-space plane are constructed by using eigenvectors as the column arrays as shown in the following equations. For example, the first column of the similar matrix of diagonalization, $[-\sqrt{\mu}\xi_y/\sqrt{\varepsilon}\alpha, \sqrt{\mu}\,(\xi_x^2 + \xi_z^2)/\sqrt{\varepsilon}\xi_x\alpha, \sqrt{\mu}\xi_y\xi_z/\sqrt{\varepsilon}\xi_x\alpha, -\xi_y/\xi_x, 0, 1]$, in the ξ-t plane is the eigenvector corresponding to the eigenvalue of $\lambda_\xi = -\alpha/V\sqrt{\varepsilon\mu}$. Since the similar matrices of diagonalization, S_ξ, S_η, and S_ζ, are non-singular, the left-hand inverse matrices, S_ξ^{-1}, S_η^{-1}, and S_ζ^{-1} are easily found. They are displayed as

$$S_\xi = \begin{bmatrix} -\frac{\sqrt{\mu}\xi_y}{\sqrt{\varepsilon}\alpha} & \frac{\sqrt{\mu}\xi_z}{\sqrt{\varepsilon}\alpha} & \frac{\sqrt{\mu}\xi_y}{\sqrt{\varepsilon}\alpha} & -\frac{\sqrt{\mu}\xi_z}{\sqrt{\varepsilon}\alpha} & 1 & 0 \\ \frac{\sqrt{\mu}(\xi_x^2+\xi_z^2)}{\sqrt{\varepsilon}\xi_x\alpha} & \frac{\sqrt{\mu}\xi_y\xi_z}{\sqrt{\varepsilon}\xi_x\alpha} & -\frac{\sqrt{\mu}(\xi_x^2+\xi_z^2)}{\sqrt{\varepsilon}\xi_x\alpha} & -\frac{\sqrt{\mu}\xi_y\xi_z}{\sqrt{\varepsilon}\xi_x\alpha} & \frac{\xi_y}{\xi_x} & 0 \\ -\frac{\sqrt{\mu}\xi_y\xi_z}{\sqrt{\varepsilon}\xi_x\alpha} & -\frac{\sqrt{\mu}(\xi_x^2+\xi_y^2)}{\sqrt{\varepsilon}\xi_x\alpha} & \frac{\sqrt{\mu}\xi_y\xi_z}{\sqrt{\varepsilon}\xi_x\alpha} & \frac{\sqrt{\mu}(\xi_x^2+\xi_y^2)}{\sqrt{\varepsilon}\xi_x\alpha} & \frac{\xi_z}{\xi_x} & 0 \\ -\frac{\xi_z}{\xi_x} & -\frac{\xi_y}{\xi_x} & -\frac{\xi_z}{\xi_x} & -\frac{\xi_y}{\xi_x} & 0 & 1 \\ 0 & 1 & 0 & 1 & 0 & \frac{\xi_y}{\xi_x} \\ 1 & 0 & 1 & 0 & 0 & \frac{\xi_z}{\xi_x} \end{bmatrix} \tag{16}$$

$$S_\eta = \begin{bmatrix} -\frac{(\eta_y^2+\eta_z^2)\sqrt{\mu}}{\sqrt{\varepsilon}\eta_y\beta} & -\frac{\eta_x\eta_z\sqrt{\mu}}{\sqrt{\varepsilon}\eta_y\beta} & \frac{(\eta_y^2+\eta_z^2)\sqrt{\mu}}{\sqrt{\varepsilon}\eta_y\beta} & \frac{\eta_x\eta_z\sqrt{\mu}}{\sqrt{\varepsilon}\eta_y\beta} & \frac{\eta_x}{\eta_y} & 0 \\ \frac{\eta_x\sqrt{\mu}}{\sqrt{\varepsilon}\beta} & -\frac{\eta_z\sqrt{\mu}}{\sqrt{\varepsilon}\beta} & -\frac{\eta_x\sqrt{\mu}}{\sqrt{\varepsilon}\beta} & \frac{\eta_z\sqrt{\mu}}{\sqrt{\varepsilon}\beta} & 1 & 0 \\ \frac{\eta_x\eta_z\sqrt{\mu}}{\sqrt{\varepsilon}\eta_y\beta} & \frac{(\eta_x^2+\eta_y^2)\sqrt{\mu}}{\sqrt{\varepsilon}\eta_y\beta} & -\frac{\eta_x\eta_z\sqrt{\mu}}{\sqrt{\varepsilon}\eta_y\beta} & -\frac{(\eta_x^2+\eta_y^2)\sqrt{\mu}}{\sqrt{\varepsilon}\eta_y\beta} & \frac{\eta_z}{\eta_y} & 0 \\ 0 & 1 & 0 & 1 & 0 & \frac{\eta_x}{\eta_y} \\ -\frac{\eta_z}{\eta_y} & -\frac{\eta_x}{\eta_y} & -\frac{\eta_z}{\eta_y} & -\frac{\eta_x}{\eta_y} & 0 & 1 \\ 1 & 0 & 1 & 0 & 0 & \frac{\eta_z}{\eta_y} \end{bmatrix} \tag{17}$$

$$S_\zeta = \begin{bmatrix} \frac{\sqrt{\mu}(\zeta_y^2+\zeta_z^2)}{\sqrt{\varepsilon}\zeta_z\gamma} & \frac{\sqrt{\mu}\zeta_x\zeta_y}{\sqrt{\varepsilon}\zeta_z\gamma} & -\frac{\sqrt{\mu}(\zeta_y^2+\zeta_z^2)}{\sqrt{\varepsilon}\zeta_z\gamma} & -\frac{\sqrt{\mu}\zeta_x\zeta_y}{\sqrt{\varepsilon}\zeta_z\gamma} & \frac{\zeta_x}{\zeta_z} & 0 \\ -\frac{\sqrt{\mu}\zeta_x\zeta_y}{\sqrt{\varepsilon}\zeta_z\gamma} & -\frac{\sqrt{\mu}(\zeta_x^2+\zeta_z^2}{\sqrt{\varepsilon}\zeta_z\gamma} & \frac{\sqrt{\mu}\zeta_x\zeta_y}{\sqrt{\varepsilon}\zeta_z\gamma} & \frac{\sqrt{\mu}(\zeta_x^2+\zeta_z^2}{\sqrt{\varepsilon}\zeta_z\gamma} & \frac{\zeta_y}{\zeta_z} & 0 \\ -\frac{\sqrt{\mu}\zeta_x}{\sqrt{\varepsilon}\gamma} & \frac{\sqrt{\mu}\zeta_y}{\sqrt{\varepsilon}\gamma} & \frac{\sqrt{\mu}\zeta_x}{\sqrt{\varepsilon}\gamma} & -\frac{\sqrt{\mu}\zeta_y}{\sqrt{\varepsilon}\gamma} & 1 & 0 \\ 0 & 1 & 0 & 1 & 0 & \frac{\zeta_x}{\zeta_z} \\ 1 & 0 & 1 & 0 & 0 & \frac{\zeta_y}{\zeta_z} \\ -\frac{\zeta_y}{\zeta_z} & -\frac{\zeta_x}{\zeta_z} & -\frac{\zeta_y}{\zeta_z} & -\frac{\zeta_x}{\zeta_z} & 0 & 1 \end{bmatrix} \tag{18}$$

$$S_\xi^{-1} = \begin{bmatrix} \frac{-(\sqrt{\varepsilon}\xi_y)}{2\sqrt{\mu}\alpha} & \frac{\sqrt{\varepsilon}\xi_x}{2\sqrt{\mu}\alpha} & 0 & \frac{-(\xi_x\xi_z)}{2\alpha^2} & \frac{-(\xi_y\xi_z)}{2\alpha^2} & \frac{\xi_x^2+\xi_y^2}{2\alpha^2} \\ \frac{\sqrt{\varepsilon}\xi_z}{2\sqrt{\mu}\alpha} & 0 & \frac{-(\sqrt{\varepsilon}\xi_x)}{2\sqrt{\mu}\alpha} & \frac{-(\xi_x\xi_y)}{2\alpha^2} & \frac{\xi_x^2+\xi_z^2}{2\alpha^2} & \frac{-(\xi_y\xi_z)}{2\alpha^2} \\ \frac{\sqrt{\varepsilon}\xi_y}{2\sqrt{\mu}\alpha} & \frac{-(\sqrt{\varepsilon}\xi_x)}{2\sqrt{\mu}\alpha} & 0 & \frac{-(\xi_x\xi_z)}{2\alpha^2} & \frac{-(\xi_y\xi_z)}{2\alpha^2} & \frac{\xi_x^2+\xi_y^2}{2\alpha^2} \\ \frac{-(\sqrt{\varepsilon}\xi_z)}{2\sqrt{\mu}\alpha} & 0 & \frac{\sqrt{\varepsilon}\xi_x}{2\sqrt{\mu}\alpha} & \frac{-(\xi_x\xi_y)}{2\alpha^2} & \frac{\xi_x^2+\xi_z^2}{2\alpha^2} & \frac{-(\xi_y\xi_z)}{2\alpha^2} \\ \frac{\xi_x^2}{\alpha^2} & \frac{\xi_x\xi_y}{\alpha^2} & \frac{\xi_x\xi_z}{\alpha^2} & 0 & 0 & 0 \\ 0 & 0 & 0 & \frac{\xi_x^2}{\alpha^2} & \frac{\xi_x\xi_y}{\alpha^2} & \frac{\xi_x\xi_z}{\alpha^2} \end{bmatrix} \tag{19}$$

$$S_\eta^{-1} = \begin{bmatrix} \frac{-(\sqrt{\varepsilon}\eta_y)}{2\beta\sqrt{\mu}} & \frac{\sqrt{\varepsilon}\eta_x}{2\beta\sqrt{\mu}} & 0 & \frac{-(\eta_x\eta_z)}{2\beta^2} & \frac{-(\eta_y\eta_z)}{2\beta^2} & \frac{\eta_x^2+\eta_y^2}{2\beta^2} \\ 0 & \frac{-(\sqrt{\varepsilon}\eta_z)}{2\beta\sqrt{\mu}} & \frac{\sqrt{\varepsilon}\eta_y}{2\beta\sqrt{\mu}} & \frac{\eta_y^2+\eta_z^2}{2\beta^2} & \frac{-(\eta_x\eta_y)}{2\beta^2} & \frac{-(\eta_x\eta_z)}{2\beta^2} \\ \frac{\sqrt{\varepsilon}\eta_y}{2\beta\sqrt{\mu}} & \frac{-(\sqrt{\varepsilon}\eta_x)}{2\beta\sqrt{\mu}} & 0 & \frac{-(\eta_x\eta_z)}{2\beta^2} & \frac{-(\eta_y\eta_z)}{2\beta^2} & \frac{\eta_x^2+\eta_y^2}{2\beta^2} \\ 0 & \frac{\sqrt{\varepsilon}\eta_z}{2\beta\sqrt{\mu}} & \frac{-(\sqrt{\varepsilon}\eta_y)}{2\beta\sqrt{\mu}} & \frac{\eta_y^2+\eta_z^2}{2\beta^2} & \frac{-(\eta_x\eta_y)}{2\beta^2} & \frac{-(\eta_x\eta_z)}{2\beta^2} \\ \frac{\eta_x\eta_y}{\beta^2} & \frac{\eta_y^2}{\beta^2} & \frac{\eta_y\eta_z}{\beta^2} & 0 & 0 & 0 \\ 0 & 0 & 0 & \frac{\eta_x\eta_y}{\beta^2} & \frac{\eta_y^2}{\beta^2} & \frac{\eta_y\eta_z}{\beta^2} \end{bmatrix} \tag{20}$$

$$S_\zeta^{-1} = \begin{bmatrix} \frac{\sqrt{\varepsilon}\zeta_z}{2\sqrt{\mu}\gamma} & 0 & \frac{-(\sqrt{\varepsilon}\zeta_x)}{2\sqrt{\mu}\gamma} & \frac{-(\zeta_x\zeta_y)}{2\gamma^2} & \frac{\zeta_x^2+\zeta_z^2}{2\gamma^2} & \frac{-(\zeta_y\zeta_z)}{2\gamma^2} \\ 0 & \frac{-(\sqrt{\varepsilon}\zeta_z)}{2\sqrt{\mu}\gamma} & \frac{\sqrt{\varepsilon}\zeta_y}{2\sqrt{\mu}\gamma} & \frac{\zeta_y^2+\zeta_z^2}{2\gamma^2} & \frac{-(\zeta_x\zeta_y)}{2\gamma^2} & \frac{-(\zeta_x\zeta_z)}{2\gamma^2} \\ \frac{-(\sqrt{\varepsilon}\zeta_z)}{2\sqrt{\mu}\gamma} & 0 & \frac{\sqrt{\varepsilon}\zeta_x}{2\sqrt{\mu}\gamma} & \frac{-(\zeta_x\zeta_y)}{2\gamma^2} & \frac{\zeta_x^2+\zeta_z^2}{2\gamma^2} & \frac{-(\zeta_y\zeta_z)}{2\gamma^2} \\ 0 & \frac{\sqrt{\varepsilon}\zeta_z}{2\sqrt{\mu}\gamma} & \frac{-(\sqrt{\varepsilon}\zeta_y)}{2\sqrt{\mu}\gamma} & \frac{\zeta_y^2+\zeta_z^2}{2\gamma^2} & \frac{-(\zeta_x\zeta_y)}{2\gamma^2} & \frac{-(\zeta_x\zeta_z)}{2\gamma^2} \\ \frac{\zeta_x\zeta_z}{\gamma^2} & \frac{\zeta_y\zeta_z}{\gamma^2} & \frac{\zeta_z^2}{\gamma^2} & 0 & 0 & 0 \\ 0 & 0 & 0 & \frac{\zeta_x\zeta_z}{\gamma^2} & \frac{\zeta_y\zeta_z}{\gamma^2} & \frac{\zeta_z^2}{\gamma^2} \end{bmatrix}. \tag{21}$$

In order to achieve the Riemann formulation, the differential system must be homogeneous and the coefficients of equations must also be invariant with respect to the independent variables [9]. In the transformed space, eigenvalues and eigenvectors of the Maxwell equations contain metrics of coordinate transformation which are position dependent. Now the left-hand inverse matrices S_ξ^{-1}, S_η^{-1}, and S_ζ^{-1} can no longer be brought into the spatial differential operator without introducing an inhomogeneous term. Therefore, the characteristic based formulation on curvilinear coordinates becomes an approximation to the Riemann problem [4, 5, 9].

IV. FLUX VECTOR SPLITTING

An efficient flux vector splitting algorithm for solving the Euler equations was developed by Steger and Warming [19]. The basic concept is equally applicable to any hyperbolic differential system for which the solution may not necessarily be analytic [9, 11]. For inviscid-flow simulations in computational fluid dynamics, the governing equations are quasi-linear and the eigenvalues are functions of dependent variables. The formulation is at best an approximate Riemann problem [11]. Numerical oscillations have appeared in calculated results using the flux vector splitting technique when eigenvalues change sign. A refined flux difference splitting algorithm with a limiter has been developed to resolve fields with jump conditions [12, 13]. The newer flux difference splitting algorithm is particularly effective at points where the eigenvalues vanish. In most computational electromagnetics applications, the jump conditions are associated with interfaces of media. The magnitude of change across the interface is also much less drastic than the shock waves encountered in supersonic flows. Perhaps more crucial for electromagnetics, the polarization of the medium occurs only in the extremely high frequency range [16, 17]. In general the governing equations are linear and the eigenvalues of the differential system are independent of the electromagnetic field. For this reason, the difference between the flux vector splitting and flux difference splitting schemes when applied to the time-dependent Maxwell equations is not overly significant.

The basic idea of the flux vector splitting of Steger and Warming is to process data according to the direction of information propagation [19]. The flux vectors are computed by the point value, including the metrics at the node of interest. This formulation for solving hyperbolic partial differential equations not only ensures the well-posedness of the differential system, but also enhances the stability of the numerical procedure [4, 11]. Specifically, the flux vectors F_ξ, F_η, and F_ζ will be split according to the sign of their corresponding eigenvalues. The split fluxes are differenced by an upwind algorithm to honor the zone of dependence for an initial-value problem.

The split flux of the three-dimensional Maxwell equations is not unique, but the sum of the split components must be unambiguously identical to the flux vector of the governing equation (7). In the present analysis, the eigenvectors are selected in such a fashion that the matrices of similarity transformation will degenerate to the form of the Cartesian frame [5, 10]. All flux vectors are split according to the signs of the eigenvalues:

$$F_\xi = F_\xi^+ + F_\xi^- \tag{22}$$

$$F_\eta = F_\eta^+ + F_\eta^- \tag{23}$$

$$F_\zeta = F_\zeta^+ + F_\zeta^- . \tag{24}$$

The flux vector components associated with the positive and negative eigenvalue are obtainable by straightforward matrix multiplication:

$$\begin{aligned} F_\xi^+ &= S_\xi \lambda_\xi^+ S_\xi^{-1} U \\ F_\xi^- &= S_\xi \lambda_\xi^- S_\xi^{-1} U \end{aligned} \tag{25}$$

$$\begin{aligned} F_\eta^+ &= S_\eta \lambda_\eta^+ S_\eta^{-1} U \\ F_\eta^- &= S_\eta \lambda_\eta^- S_\eta^{-1} U \end{aligned} \tag{26}$$

$$\begin{aligned} F_\zeta^+ &= S_\zeta \lambda_\zeta^+ S_\zeta^{-1} U \\ F_\zeta^- &= S_\zeta \lambda_\zeta^- S_\zeta^{-1} U. \end{aligned} \tag{27}$$

The split flux vectors in the respective ξ–t, η–t, and ζ–t planes are obtained by straightforward matrix multiplication and are given as

$$F_\xi^+ = \begin{bmatrix} \frac{\xi_y^2+\xi_z^2}{2\sqrt{\varepsilon\mu}V\alpha} & \frac{-(\xi_x\xi_y)}{2\sqrt{\varepsilon\mu}V\alpha} & \frac{-(\xi_x\xi_z)}{2\sqrt{\varepsilon\mu}V\alpha} & 0 & \frac{-\xi_z}{2\varepsilon V} & \frac{\xi_y}{2\varepsilon V} \\ \frac{-(\xi_x\xi_y)}{2\sqrt{\varepsilon\mu}V\alpha} & \frac{\xi_x^2+\xi_z^2}{2\sqrt{\varepsilon\mu}V\alpha} & \frac{-(\xi_y\xi_z)}{2\sqrt{\varepsilon\mu}V\alpha} & \frac{\xi_z}{2\varepsilon V} & 0 & \frac{-\xi_x}{2\varepsilon V} \\ \frac{-(\xi_x\xi_z)}{2\sqrt{\varepsilon\mu}V\alpha} & \frac{-(\xi_y\xi_z)}{2\sqrt{\varepsilon\mu}V\alpha} & \frac{\xi_x^2+\xi_y^2}{2\sqrt{\varepsilon\mu}V\alpha} & \frac{-\xi_y}{2\varepsilon V} & \frac{\xi_x}{2\varepsilon V} & 0 \\ 0 & \frac{\xi_z}{2V\mu} & \frac{-\xi_y}{2V\mu} & \frac{\xi_y^2+\xi_z^2}{2\sqrt{\varepsilon\mu}V\alpha} & \frac{-(\xi_x\xi_y)}{2\sqrt{\varepsilon\mu}V\alpha} & \frac{-(\xi_x\xi_z)}{2\sqrt{\varepsilon\mu}V\alpha} \\ \frac{-\xi_z}{2V\mu} & 0 & \frac{\xi_x}{2V\mu} & \frac{-(\xi_x\xi_y)}{2\sqrt{\varepsilon\mu}V\alpha} & \frac{\xi_x^2+\xi_z^2}{2\sqrt{\varepsilon\mu}V\alpha} & \frac{-(\xi_y\xi_z)}{2\sqrt{\varepsilon\mu}V\alpha} \\ \frac{\xi_y}{2V\mu} & \frac{-\xi_x}{2V\mu} & 0 & \frac{-(\xi_x\xi_z)}{2\sqrt{\varepsilon\mu}V\alpha} & \frac{-(\xi_y\xi_z)}{2\sqrt{\varepsilon\mu}V\alpha} & \frac{\xi_x^2+\xi_y^2}{2\sqrt{\varepsilon\mu}V\alpha} \end{bmatrix} \begin{Bmatrix} B_x \\ B_y \\ B_z \\ D_x \\ D_y \\ D_z \end{Bmatrix} \tag{28}$$

$$F_\xi^- = \begin{bmatrix} \frac{-(\xi_y^2+\xi_z^2)}{2\sqrt{\varepsilon\mu}V\alpha} & \frac{\xi_x\xi_y}{2\sqrt{\varepsilon\mu}V\alpha} & \frac{\xi_x\xi_z}{2\sqrt{\varepsilon\mu}V\alpha} & 0 & \frac{-\xi_z}{2\varepsilon V} & \frac{\xi_y}{2\varepsilon V} \\ \frac{\xi_x\xi_y}{2\sqrt{\varepsilon\mu}V\alpha} & \frac{-(\xi_x^2+\xi_z^2)}{2\sqrt{\varepsilon\mu}V\alpha} & \frac{\xi_y\xi_z}{2\sqrt{\varepsilon\mu}V\alpha} & \frac{\xi_z}{2\varepsilon V} & 0 & \frac{-\xi_x}{2\varepsilon V} \\ \frac{\xi_x\xi_z}{2\sqrt{\varepsilon\mu}V\alpha} & \frac{\xi_y\xi_z}{2\sqrt{\varepsilon\mu}V\alpha} & \frac{-(\xi_x^2+\xi_y^2)}{2\sqrt{\varepsilon\mu}V\alpha} & \frac{-\xi_y}{2\varepsilon V} & \frac{\xi_x}{2\varepsilon V} & 0 \\ 0 & \frac{\xi_z}{2V\mu} & \frac{-\xi_y}{2V\mu} & \frac{-(\xi_y^2+\xi_z^2)}{2\sqrt{\varepsilon\mu}V\alpha} & \frac{\xi_x\xi_y}{2\sqrt{\varepsilon\mu}V\alpha} & \frac{\xi_x\xi_z}{2\sqrt{\varepsilon\mu}V\alpha} \\ \frac{-\xi_z}{2V\mu} & 0 & \frac{\xi_x}{2V\mu} & \frac{\xi_x\xi_y}{2\sqrt{\varepsilon\mu}V\alpha} & \frac{-(\xi_x^2+\xi_z^2)}{2\sqrt{\varepsilon\mu}V\alpha} & \frac{\xi_y\xi_z}{2\sqrt{\varepsilon\mu}V\alpha} \\ \frac{\xi_y}{2V\mu} & \frac{-\xi_x}{2V\mu} & 0 & \frac{\xi_x\xi_z}{2\sqrt{\varepsilon\mu}V\alpha} & \frac{\xi_y\xi_z}{2\sqrt{\varepsilon\mu}V\alpha} & \frac{-(\xi_x^2+\xi_y^2)}{2\sqrt{\varepsilon\mu}V\alpha} \end{bmatrix} \begin{Bmatrix} B_x \\ B_y \\ B_z \\ D_x \\ D_y \\ D_z \end{Bmatrix} \tag{29}$$

$$F_\eta^+ = \begin{bmatrix} \frac{\eta_y^2+\eta_z^2}{2\sqrt{\varepsilon\mu}\beta V} & \frac{-(\eta_x\eta_y)}{2\sqrt{\varepsilon\mu}\beta V} & \frac{-(\eta_x\eta_z)}{2\sqrt{\varepsilon\mu}\beta V} & 0 & \frac{-\eta_z}{2\varepsilon V} & \frac{\eta_y}{2\varepsilon V} \\ \frac{-(\eta_x\eta_y)}{2\sqrt{\varepsilon\mu}\beta V} & \frac{\eta_x^2+\eta_z^2}{2\sqrt{\varepsilon\mu}\beta V} & \frac{-(\eta_y\eta_z)}{2\sqrt{\varepsilon\mu}\beta V} & \frac{\eta_z}{2\varepsilon V} & 0 & \frac{-\eta_x}{2\varepsilon V} \\ \frac{-(\eta_x\eta_z)}{2\sqrt{\varepsilon\mu}\beta V} & \frac{-(\eta_y\eta_z)}{2\sqrt{\varepsilon\mu}\beta V} & \frac{\eta_x^2+\eta_y^2}{2\sqrt{\varepsilon\mu}\beta V} & \frac{-\eta_y}{2\varepsilon V} & \frac{\eta_x}{2\varepsilon V} & 0 \\ 0 & \frac{\eta_z}{2V\mu} & \frac{-\eta_y}{2V\mu} & \frac{\eta_y^2+\eta_z^2}{2\sqrt{\varepsilon\mu}\beta V} & \frac{-(\eta_x\eta_y)}{2\sqrt{\varepsilon\mu}\beta V} & \frac{-(\eta_x\eta_z)}{2\sqrt{\varepsilon\mu}\beta V} \\ \frac{-\eta_z}{2V\mu} & 0 & \frac{\eta_x}{2V\mu} & \frac{-(\eta_x\eta_y)}{2\sqrt{\varepsilon\mu}\beta V} & \frac{\eta_x^2+\eta_z^2}{2\sqrt{\varepsilon\mu}\beta V} & \frac{-(\eta_y\eta_z)}{2\sqrt{\varepsilon\mu}\beta V} \\ \frac{\eta_y}{2V\mu} & \frac{-\eta_x}{2V\mu} & 0 & \frac{-(\eta_x\eta_z)}{2\sqrt{\varepsilon\mu}\beta V} & \frac{-(\eta_y\eta_z)}{2\sqrt{\varepsilon\mu}\beta V} & \frac{\eta_x^2+\eta_y^2}{2\sqrt{\varepsilon\mu}\beta V} \end{bmatrix} \begin{Bmatrix} B_x \\ B_y \\ B_z \\ D_x \\ D_y \\ D_z \end{Bmatrix} \tag{30}$$

$$F_\eta^- = \begin{bmatrix} \frac{-(\eta_y^2+\eta_z^2)}{2\sqrt{\varepsilon\mu}\beta V} & \frac{\eta_x\eta_y}{2\sqrt{\varepsilon\mu}\beta V} & \frac{\eta_x\eta_z}{2\sqrt{\varepsilon\mu}\beta V} & 0 & \frac{-\eta_z}{2\varepsilon V} & \frac{\eta_y}{2\varepsilon V} \\ \frac{\eta_x\eta_y}{2\sqrt{\varepsilon\mu}\beta V} & \frac{-(\eta_x^2+\eta_z^2)}{2\sqrt{\varepsilon\mu}\beta V} & \frac{\eta_y\eta_z}{2\sqrt{\varepsilon\mu}\beta V} & \frac{\eta_z}{2\varepsilon V} & 0 & \frac{-\eta_x}{2\varepsilon V} \\ \frac{\eta_x\eta_z}{2\sqrt{\varepsilon\mu}\beta V} & \frac{\eta_y\eta_z}{2\sqrt{\varepsilon\mu}\beta V} & \frac{-(\eta_x^2+\eta_y^2)}{2\sqrt{\varepsilon\mu}\beta V} & \frac{-\eta_y}{2\varepsilon V} & \frac{\eta_x}{2\varepsilon V} & 0 \\ 0 & \frac{\eta_z}{2V\mu} & \frac{-\eta_y}{2V\mu} & \frac{-(\eta_y^2+\eta_z^2)}{2\sqrt{\varepsilon\mu}\beta V} & \frac{\eta_x\eta_y}{2\sqrt{\varepsilon\mu}\beta V} & \frac{\eta_x\eta_z}{2\sqrt{\varepsilon\mu}\beta V} \\ \frac{-\eta_z}{2V\mu} & 0 & \frac{\eta_x}{2V\mu} & \frac{\eta_x\eta_y}{2\sqrt{\varepsilon\mu}\beta V} & \frac{-(\eta_x^2+\eta_z^2)}{2\sqrt{\varepsilon\mu}\beta V} & \frac{\eta_y\eta_z}{2\sqrt{\varepsilon\mu}\beta V} \\ \frac{\eta_y}{2V\mu} & \frac{-\eta_x}{2V\mu} & 0 & \frac{\eta_x\eta_z}{2\sqrt{\varepsilon\mu}\beta V} & \frac{\eta_y\eta_z}{2\sqrt{\varepsilon\mu}\beta V} & \frac{-(\eta_x^2+\eta_y^2)}{2\sqrt{\varepsilon\mu}\beta V} \end{bmatrix} \begin{Bmatrix} B_x \\ B_y \\ B_z \\ D_x \\ D_y \\ D_z \end{Bmatrix} \tag{31}$$

$$F_\zeta^+ = \begin{bmatrix} \frac{\zeta_y^2+\zeta_z^2}{2\sqrt{\varepsilon\mu}V\gamma} & \frac{-(\zeta_x\zeta_y)}{2\sqrt{\varepsilon\mu}V\gamma} & \frac{-(\zeta_x\zeta_z)}{2\sqrt{\varepsilon\mu}V\gamma} & 0 & \frac{-\zeta_z}{2\varepsilon V} & \frac{\zeta_y}{2\varepsilon V} \\ \frac{-(\zeta_x\zeta_y)}{2\sqrt{\varepsilon\mu}V\gamma} & \frac{\zeta_x^2+\zeta_z^2}{2\sqrt{\varepsilon\mu}V\gamma} & \frac{-(\zeta_y\zeta_z)}{2\sqrt{\varepsilon\mu}V\gamma} & \frac{\zeta_z}{2\varepsilon V} & 0 & \frac{-\zeta_x}{2\varepsilon V} \\ \frac{-(\zeta_x\zeta_z)}{2\sqrt{\varepsilon\mu}V\gamma} & \frac{-(\zeta_y\xi_z)}{2\sqrt{\varepsilon\mu}V\gamma} & \frac{\zeta_x^2+\zeta_y^2}{2\sqrt{\varepsilon\mu}V\gamma} & \frac{-\zeta_y}{2\varepsilon V} & \frac{\zeta_x}{2\varepsilon V} & 0 \\ 0 & \frac{\zeta_z}{2V\mu} & \frac{-\zeta_y}{2V\mu} & \frac{\zeta_y^2+\zeta_z^2}{2\sqrt{\varepsilon\mu}V\gamma} & \frac{-(\zeta_x\zeta_y)}{2\sqrt{\varepsilon\mu}V\gamma} & \frac{-(\zeta_x\zeta_z)}{2\sqrt{\varepsilon\mu}V\gamma} \\ \frac{-\zeta_z}{2V\mu} & 0 & \frac{\zeta_x}{2V\mu} & \frac{-(\zeta_x\zeta_y)}{2\sqrt{\varepsilon\mu}V\gamma} & \frac{\zeta_x^2+\zeta_z^2}{2\sqrt{\varepsilon\mu}V\gamma} & \frac{-(\zeta_y\zeta_z)}{2\sqrt{\varepsilon\mu}V\gamma} \\ \frac{\zeta_y}{2V\mu} & \frac{-\zeta_x}{2V\mu} & 0 & \frac{-(\zeta_x\zeta_z)}{2\sqrt{\varepsilon\mu}V\gamma} & \frac{-(\zeta_y\zeta_z)}{2\sqrt{\varepsilon\mu}V\gamma} & \frac{(\zeta_x^2+\zeta_y^2)}{2\sqrt{\varepsilon\mu}V\gamma} \end{bmatrix} \begin{Bmatrix} B_x \\ B_y \\ B_z \\ D_x \\ D_y \\ D_z \end{Bmatrix} \tag{32}$$

$$F_\zeta^- = \begin{bmatrix} \frac{-(\zeta_y^2+\zeta_z^2)}{2\sqrt{\varepsilon\mu}V\gamma} & \frac{\zeta_x\zeta_y}{2\sqrt{\varepsilon\mu}V\gamma} & \frac{\zeta_x\zeta_z}{2\sqrt{\varepsilon\mu}V\gamma} & 0 & \frac{-\zeta_z}{2\varepsilon V} & \frac{\zeta_y}{2\varepsilon V} \\ \frac{\zeta_x\zeta_y}{2\sqrt{\varepsilon\mu}V\gamma} & \frac{-(\zeta_x^2+\zeta_z^2)}{2\sqrt{\varepsilon\mu}V\gamma} & \frac{\zeta_y\zeta_z}{2\sqrt{\varepsilon\mu}V\gamma} & \frac{\zeta_z}{2\varepsilon V} & 0 & \frac{-\zeta_x}{2\varepsilon V} \\ \frac{\zeta_x\zeta_z}{2\sqrt{\varepsilon\mu}V\gamma} & \frac{\zeta_y\xi_z}{2\sqrt{\varepsilon\mu}V\gamma} & \frac{-(\zeta_x^2+\zeta_y^2)}{2\sqrt{\varepsilon\mu}V\gamma} & \frac{-\zeta_y}{2\varepsilon V} & \frac{\zeta_x}{2\varepsilon V} & 0 \\ 0 & \frac{\zeta_z}{2V\mu} & \frac{-\zeta_y}{2V\mu} & \frac{-(\zeta_y^2+\zeta_z^2)}{2\sqrt{\varepsilon\mu}V\gamma} & \frac{\zeta_x\zeta_y}{2\sqrt{\varepsilon\mu}V\gamma} & \frac{\zeta_x\zeta_z}{2\sqrt{\varepsilon\mu}V\gamma} \\ \frac{-\zeta_z}{2V\mu} & 0 & \frac{\zeta_x}{2V\mu} & \frac{\zeta_x\zeta_y}{2\sqrt{\varepsilon\mu}V\gamma} & \frac{-(\zeta_x^2+\zeta_z^2)}{2\sqrt{\varepsilon\mu}V\gamma} & \frac{\zeta_y\zeta_z}{2\sqrt{\varepsilon\mu}V\gamma} \\ \frac{\zeta_y}{2V\mu} & \frac{-\zeta_x}{2V\mu} & 0 & \frac{\zeta_x\zeta_z}{2\sqrt{\varepsilon\mu}V\gamma} & \frac{\zeta_y\zeta_z}{2\sqrt{\varepsilon\mu}V\gamma} & \frac{-(\zeta_x^2+\zeta_y^2)}{2\sqrt{\varepsilon\mu}V\gamma} \end{bmatrix} \begin{Bmatrix} B_x \\ B_y \\ B_z \\ D_x \\ D_y \\ D_z \end{Bmatrix} \tag{33}$$

Although the split flux vectors may have a wide range of variation from different selections of linearly independent eigenvectors, the present result is internally consistent. The judiciously selected eigenvectors have ensured that if the coordinate system degenerates into the Cartesian frame, the split flux vectors will reduce accordingly (4, 5). This assertion can be verified easily by observing that all elements of the split flux vectors contain the definitive metrics of coordinate transformation ξ_x, η_y, and ζ_z in the denominator. Therefore, the split flux vectors of the present effort can be adopted as the foundation for future characteristic-based finite-difference approximations to Maxwell equations in the time domain. This formulation not only permits the numerical reproduction of piecewise continuous solution, but also enhances the stability of numerical approaches [19].

V. FINITE-DIFFERENCE APPROXIMATION

Once the detailed split fluxes are known, formulation of the finite-difference approximation is straightforward. From the sign of an eigenvalue, the stencil of a spatially second-order accurate windward differencing can easily be constructed to form multiple one-dimensional difference operators [4, 5]. The split flux vectors are evaluated at each discretized point of the field according to the signs of the eigenvalues:

$$\text{If } \lambda < 0, \Delta U_i = [-3U_i + 4U_{i+1} - U_{i+2}]/2 \tag{34}$$

$$\text{If } \lambda > 0, \nabla U_i = [+3U_i - 4U_{i-1} + U_{i-2}]/2. \tag{35}$$

All metrics of the coordinate transformation are calculated by central differencing, except at the edges of the computational domain, where one-sided differencing are used. Although the fractional-step or the time-splitting algorithm [20, 21] has demonstrated greater efficiency in data storages and higher data processing rates than predictor–corrector time integration procedures [4, 5], it is not implemented here. For the purpose of comparison, the Runge–Kutta family of single-step, multi-stage procedures, is employed to be consistent with the accompanying characteristic-based finite-volume method [10, 22]. In the present effort, a two-stage, formally second order accurate scheme is used:

$$\begin{aligned} U_0 &= U_n \\ U_1 &= U_0 - \Delta U(U_0) \\ U_2 &= U_0 - 0.5(\Delta U(U_1) + \Delta U(U_0)) \\ U_{n+1} &= U_2. \end{aligned}$$

The resultant characteristic-based finite-difference scheme for solving the three-dimensional Maxwell equations in the time domain is second-order accurate in both time and space.

The most significant feature of the flux vector splitting scheme lies in its ability to easily suppress reflected waves on the truncated computational domain. In wave motion, the compatibility condition at any point in space is described by the split flux vector [4, 5, 10]. In the present formulation, an approximated no-reflection condition can be achieved by setting the incoming flux component to zero:

$$\lim_{r\to\infty} F^+ = 0 \quad \text{or} \quad \lim_{r\to\infty} F^- = 0. \tag{36}$$

The one-dimensional compatibility condition is exact when the wave motion is aligned with one of the coordinates. This unique attribute of the characteristic-based numerical

procedure in removing a fundamental dilemma in computational electromagnetics will be demonstrated in detail later.

VI. FINITE-VOLUME APPROXIMATION

The finite-volume approximation is solved for the governing equation, Eq. (7), in the discretized form

$$\frac{\Delta U}{\Delta t} + \frac{\Delta F}{\Delta \xi} + \frac{\Delta G}{\Delta \eta} + \frac{\Delta H}{\Delta \zeta} - J = 0. \tag{37}$$

In the present cell-centered finite-volume scheme, the integration procedure degenerates into balancing the flux vectors on interfaces of discretized cells [10]. In essence, the numerical procedure needs only to evaluate the sum of all flux vectors aligned with surface area vectors [10–13]. Only one of the vectors is required to coincide with the outward normal of the cell surface and the rest of the orthogonal triad can be derived to lie on the same surface. The metrics, or more appropriately the direction cosines, of any points within the cell are uniquely determined by the nodes and edges of the elementary volume. This feature is distinct from a point value derived from adjacent nodes, as in the finite-difference approximation. The shape of the cell under consideration and the stretching ratio of neighbor cells [14] can lead to a significant deterioration of the accuracy of cell-centered finite-volume schemes.

An outstanding aspect of the finite-volume scheme is the elegance of its flux splitting process.The flux difference splitting for Eq. (37) is greatly facilitated by a locally orthogonal system in the transformed space [12, 13]. In this new frame of reference, eigenvalues and eigenvectors, as well as metrics of the coordinate transformation between two orthogonal systems, are well known [4, 5]. The inverse transformation is simply the transpose of the forward mapping. Particularly, the flux vectors in the transformed space have the same functional form as that of the Cartesian frame, the difference is a known quantity and is defined by the product of the surface outward normal and the cell volume $V \times \nabla S/\|\nabla S\|$ [10]. Therefore, the flux vectors can be split in the transformed space according to the sign of the eigenvalues, but without detailed knowledge of the associated eigenvectors. For this reason, finite-volume schemes are widely used in the CFD community and led the CEM development for solving problems cast in general curvilinear coordinates.

The present formulation [10] adopts the van Leer's Kappa scheme in which different flux vectors can be reconstructed on the cell surface from the piecewise data of neighboring cells [12, 13]. The spatial accuracy of this scheme spans a range from first-order to third-order upwind biased approximations. The time integration is carried out by a two-stage Runge–Kutta method identical to that of the present finite-difference procedure [22]. The finite-volume procedure is therefore second-order accurate in time, and up to third-order accurate in space [10, 12, 13]. For the present purpose only the second-order upwinding and the third-order upwind biased options are exercised. The former is the nearest equivalent to the flux vector splitting finite-difference scheme; the latter is formally one order of magnitude more accurate in spatial resolution.

VII. NUMERICAL PROCEDURE

Wave motion confined within a three-dimensional rectangular wave guide is first simulated. For this phenomenon, the closed form solution of the time-dependent Maxwell equations is known (17, 18). The present results attempt to duplicate the commonly designated $TE_{(1,1)}$ transverse wave. Since the 3D electromagnetic wave is specified to propagate along the z coordinate, all the components of electric and magnetic fields contain a common sinusoidal function of time and z. The pertinent initial and boundary conditions are presecribed as follows: The incident wave is completely specified at the computational boundary for each time step. The vanishing F_z^- compatibility is imposed as the no-reflection condition at the exit plane. Only the x component of the magnetic flux density, B_x, is presented in Fig. 1. The second-order accurate results by both the finite-volume and the finite-difference schemes are depicted, together with the theoretical result. For simple wave propagation along a coordinate, total suppression of reflected waves is achieved by the characteristic-based schemes. The attribute of computational accuracy of the windward procedures is also reflected by the increased dissipative and dispersive errors as the wave frequency is

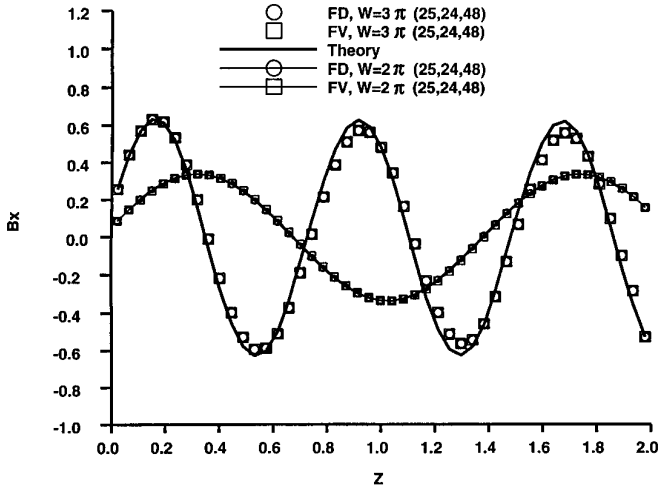

FIG. 1. Comparison of finite-difference and finite-volume solutions for a rectangular waveguide.

increased. In other words, if the time-dependent simulation is not supported by a suitable grid density, the truncation error can be significant. This behavior can be anticipated from the error analysis (12, 13). However, attention should be focused on the fact that in a regular and uniform mesh system, there is no difference in numerical behavior between these two distinctive and yet equivalent schemes.

The oscillating electric dipole is selected as the basic validation problem for which the analytic solution is known [17, 18]. At the pole, the solution is singular, which poses a severe test of algorithms in resolving steep gradients within the field. In fact, in a spherical coordinate system, the induced magnetic and electric intensities exhibit singular behavior proportional to the inverse square and cubic powers, respectively, of the radial distance, r, to coordinate origin [17, 18]. The designated radiative phenomenon is also ideal to illustrate how simply one-dimensional compatibility can be used to provide an accurate no-reflection condition on the truncated computational boundary. One-dimensioal compatibility can always be derived by a coordinate mapping in which one of the coordinates is made to align with the axis of wave motion. Since the dipole is a spherically symmetric radiating phenomenon, the electromagnetic wave is already known to propagate along the radial coordinate in the farfield. The no-reflection condition at the truncated boundary is achieved easily by setting the incoming radial flux component to zero at the two outermost nodes. Most importantly, the compatibility condition of the initial-value problem is satisfied automatically to the same order of magnitude as the solving scheme.

The initial values of the present numerical simulation are described by the analytic solution at the pole and for at least two adjacent nodes [17, 18]. The additional nodes are included to ensure that physically meaningful values are provided to the three-point windward formulation. Two more overlapping numerical boundary conditions also imposed in the azimuthal and circumferential directions. These boundary conditions are included just to meet the numerical requirement for computations.

Three mesh systems, (25, 24, 48), (37, 36, 72), and (49, 48, 96), were used to perform the comparative study. By scaling the independent and dependent variables to the ranges of unity, the coarsest mesh system does not satisfy the marginal requirement (10 nodes per wavelength) for resolving a wave motion [1, 2]. For the purpose of comparing two conceptually different numerical procedures, the finite-difference calculations were performed on nodes that are located at the cell center of the finite volume calculations. Therefore, the mesh systems between two algorithms are slightly different but within the uncertainty limit of discretization.

All computations were processed either on a Cray Y-MP8/8128 or on a C916/16256 system. For comparison of numerical efficiency, the data processing rates (DPR) and central processing unit times (CPU) required to advance the solution for one characteristic time period were recorded. The characteristic time, T_{ch}, is defined as the time required for a wave to transverse the entire computational domain. Results are shown in Table I.

TABLE I

Comparison of Numerical Performance

	FD2	FV2	FV3
YMP (25, 24, 48)			
DPR (Mflops)	105.6	132.5	148.5
Vector length	NA	NA	NA
CPT (s)	298.58	396.26	181.14
YMP (37, 36, 72)			
DPR (Mflops)	132.5	168.8	168.8
Vector length	NA	NA	NA
CPT (s)	1496.03	2315.79	1039.94
C90 (49, 48, 96)			
DPR (Mflops)	242.3	365.9	364.3
Vector length	27.7	34.7	33.4
CPT (s)	2358.25	3464.32	1558.95

In general, the third-order upwind biased scheme (FV3) is the most efficient among the three procedures investigated for two reasons. First, this scheme has a more favorable stability property than both second-order windward finite-difference (FD2) and finite-volume (FV2) procedures. The allowable time step is nearly double that of the two second-order schemes. Second, the formulation of finite volume schemes yields a greater averaged vector length (34.7 vs 27.7) in arithmetic operations than the finite difference code. The data processing rates of finite-difference and finite-volume schemes reflect the numerical advantage in vector processing by the latter. On the finest mesh, direct comparison of solutions of the two second-order windward procedures indicates that the FD2 scheme requires 46.9% less CPU time than the FV2 scheme to process the same amount of data. The FV2 procedure reveals a slightly more favorable stability property than the FD2 scheme.

VIII. DISCUSSION OF NUMERICAL RESULTS

Although the numerical simulation has been scaled to make the temporal and spatial increments of the same order of magnitude, demonstration of the formal order of numerical accuracy still has not been achieved. The uncertainty is incurred by the demanding precision in control of the allowable time steps of three numerical procedures (FD2, FV2, and FV3) on different mesh systems, and by the magnified difference of initial values via the singular behavior at the pole. Therefore, the numerical results are examined at selected locations in space, the

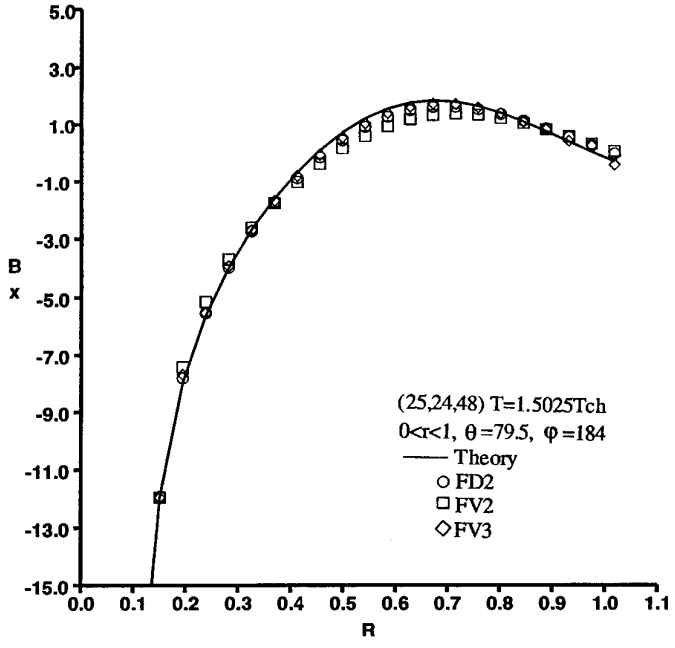

FIG. 2. Instantaneous distribution of B_x, (25, 24, 48) grid.

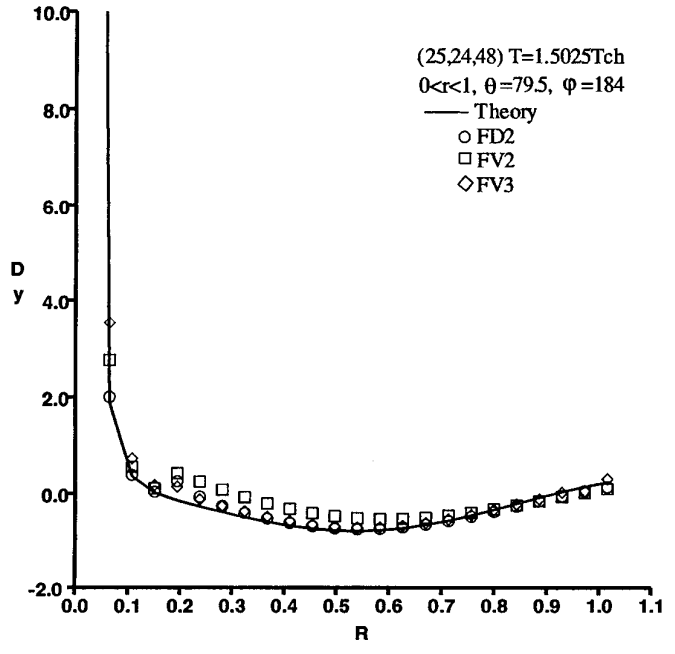

FIG. 3. Instantaneous distribution of D_y, (25, 24, 48) grid.

time trace of field variables, and a point spectral analysis. From these analyses, a superior numerical procedure will be identified and mapped onto a distributive memory multicomputers [23, 24] for engineering applications [25].

The calculated magnetic and electric components of field intensities B_x, D_y, and D_z on the coarse mesh system (25, 24, 48) are depicted in Figs. 2, 3, and 4. For the radiating problem, the z-component of the magnetic intensity is identical to zero. Numerical results correctly exhibit a value less than 10^{-10} in magnitude and are not presented. Numerical results generated by the three procedures FD2, FV2, and FV3 are collected at the instant when the time elapsed $t = 1.5025\ T_{\text{ch}}$. Data are sampled along a radial way ($\theta = 79.5$, $\phi = 184$) from near the pole to the truncated boundary. For all calculations, the initial value is specified only for mesh points that have a radial distance less than $r = 0.1513$ from the pole. The computational domain is bounded by two concentric spheres having the radii range of $0.1513 < r < 1.00$. In Fig. 2, a comparison of the computed x-component of the magnetic intensity with the theory [17, 18] is given. The results of the third-order accurate finite-volume scheme attains the best agreement with the theory as expected. Under the conditions of merely 10 cells per wavelength and $1/r^2$ singular behavior approaching the dipole, the maximum relative error is still confined to within 1%. The solution produced by the second-order windward finite-volume scheme shows a maximum discrepancy of 5.02% at $r = 0.7133$ from the theoretical result. The counterpart of the second-order finite-difference approximation performs much better. The accuracy of solution by the FD2 scheme approaches that of the formally third-order finite volume scheme, FV3.

On the coarse mesh system (25, 24, 48), the calculated electric field components are anticipated to exhibit greater disparity with respect to the theoretical value, because the theoretical result contains higher order singular behavior

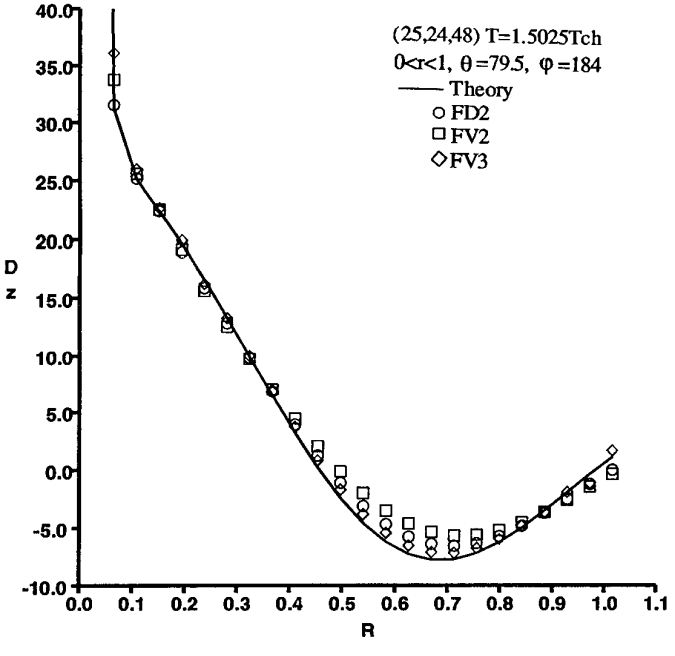

FIG. 4. Instantaneous distribution of D_z, (25, 24, 48) grid.

at the dipole than the magnetic intensity [17, 18]. The leading term of this singularity now appears as the inverse cubic power of the radial distance from the dipole. Distributions of numerical results along a radial ray indeed show a greater deviation from theory. In addition, the peculiar behavior of phase error associated with time dependent problems is now very pronounced in Fig. 3. The truncation error of computed x and y electric displacement components appears as a large shift of the computed profiles at the node immediately adjacent to which the initial values are imposed. The error pattern of the calculated results is nearly identical; thus only the y-component of the electric displacement is presented. Again in Figs. 3 and 4, the FV2 solution contains the largest error in predicting the electric field. As in the calculation of the magnetic fields, the counterpart FD2 scheme is able to generate a superior result approaching that of the FV3 scheme on spherical coordinates. Away from the inner computational boundary, the maximum error of the z-component electric field by the FV2 scheme, in Fig. 4, is located at $r = 0.6268$ and has a relative magnitude of 9.09%. This is also the greatest discrepancy observed from all calculations from the coarsest mesh system.

It may be interesting to note that in the coarsest mesh system, all results generated by the formally second-order accurate finite-difference scheme approach that of the third-order finite-volume procedure. The present numerical result seems to substantiate the assertion that the studied finite-volume procedure will suffer accuracy degradation on the excessively stretched non-rectangular quadrilateral grids [14]. In spite of that, all numerical solutions

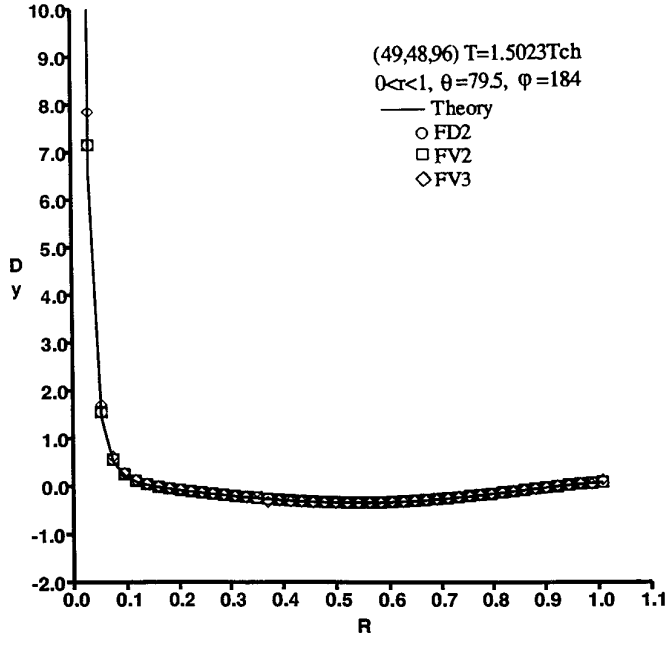

FIG. 5. Instantaneous distribution of B_x, (49, 48, 96) grid.

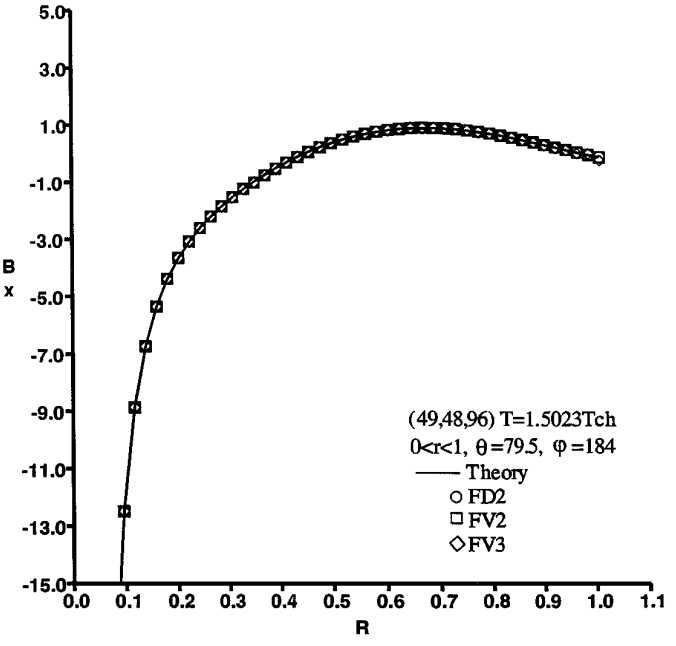

FIG. 6. Instantaneous distribution of D_y, (49, 48, 96) grid.

by both the second-order windward procedures, FV2 and FD2, suppress the reflected wave at the farfield boundary for the oscillating electric dipole. This observation can be made uniformly for all computed results of the electromagnetic field.

Refinement to a (37, 36, 72) grid, the specific comparison of numerical results yields little additional insight. Once sufficient numerical resolution is secured, the differences between numerical and theoretical results are indistinguishable in the plotting scale. Only three instantaneous field variables, the x-component of the magnetic and the y- and z-components of the electric field, are presented in Figs. 5, 6, and 7 respectively. These calculations were performed on the (49, 48, 96) grid system, and results are displayed at the instant $t = 1.5023\ T_{ch}$. In Fig. 5, the maximum discrepancy between theory and numerical results is produced by the FV2 scheme at a relative error of 0.395% at $r = 0.7332$. For the same calculation, error of the FD2 scheme is about half that of the FV2 scheme, a value of 0.211%.

The y- and z-components of the electric displacement are given in Figs. 6 and 7, respectively. The improvement of computational accuracy is clearly demonstrated by the grid point density enrichment. In Fig. 6, the FD2 scheme exhibits a slightly better predicted value than the FV2 scheme, a small difference of less than 0.9% from the exact local result [18, 19]. Fig. 7 depicts the role reversal in numerical error generation by the two second-order schemes. The maximal disparity in calculating the z-component of the electric field is generated by the FD2 scheme

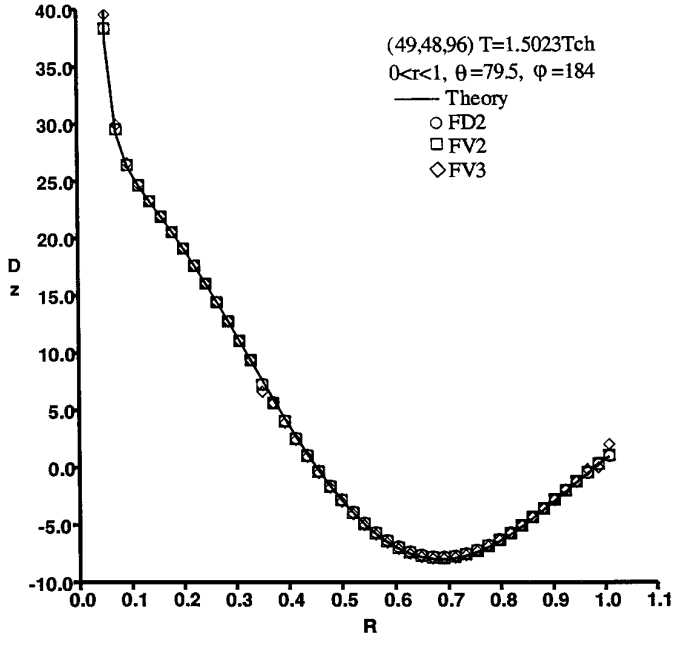

FIG. 7. Instantaneous distribution of D_z, (49, 48, 96) grid.

with a value of 2.404% at $r = 0.6268$, and the error of the counterpart FV2 scheme is only half the value. In short, if at least 15 nodes per wavelength are provided for resolving the wave motion, the second-order finite-difference and the finite-volume procedure have results of comparable accuracy.

The most important feature of eliminating reflected waves from the truncated boundary by the characteristic-based numerical procedure is repeatedly demonstrated in Figs. 5, 6, and 7. The second-order accurate windward procedures, in either the finite-volume or the finite-difference approach, use the precise stencil needed to enforce the zone of dependency according to the characteristic theory. The compatibility condition is met by simply imposing a vanishing incoming flux component at the truncated boundary. Within the limit of truncation error, no reflected wave from the farfield boundary is detected. This observation can be made uniformly from all comparisons of these instantaneous numerical simulations with theory at the truncated boundary, $r = 1.0$. On the other hand, the third-order windward-biased scheme reconstructs the split flux on an interface by an interpolation process which includes data beyond the physical domain of dependence [10, 12, 13]. The perfect no-reflection condition is not achieved. Sustained research efforts will be devoted to this issue until it is resolved.

The temporal variation of all simulated electromagnetic field components is very similar. Therefore, only two typical samplings of the time traces at a field point for a duration of 2.35 T_{ch} are given. In Fig. 8, the time traces of the computed z-component electric intensities near the middle field ($r = 0.4107$, $\theta = 79.5$, $\phi = 184$) are depicted together with the theoretical values on the (25, 24, 48) grid system. The transient period for propagating data to reach the sampling point is clearly illustrated. The two second-order windward procedures, FD2 and FV2, receive and transmit the directional information simultaneously at the sampled physical location and the third-order finite-volume scheme shows a slight delay. As it has been pointed out earlier, the FV2 scheme produces the greatest dissipative and phase error on the coarsest mesh system. All numerical procedures, FD2, FV2, and FV3, reveal a leading phase error at a time-step size $\Delta t = 1.02436 \times 10^{-3}$ s.

On the finest mesh system (49, 48, 96), the time trace of the z-component of the electric intensity at the point ($r = 0.4144$, $\theta = 79.5$, $\phi = 184$) is presented in Fig. 9. The basic numerical behavior is very similar to that observed in the coarsest mesh computations, except that the deviation from theory is much smaller. The difference among the three investigated numerical results is indistinguishable on the plotting scale. All numerical results duplicate accurately the theoretical value after an elapsed time of 1.35 T_{ch}. After the transient period, the amplitude of the wave motion is sustained within a fraction of one percent of the theoretical value and the relative leading phase error is negligible.

In order to obtain a quantified comparison of the characteristic-based schems on three mesh systems, a point spectral analysis is performed. Through this analysis, the truncation error of the numerical results can be studied to determine the dissipative and the dispersive behavior at

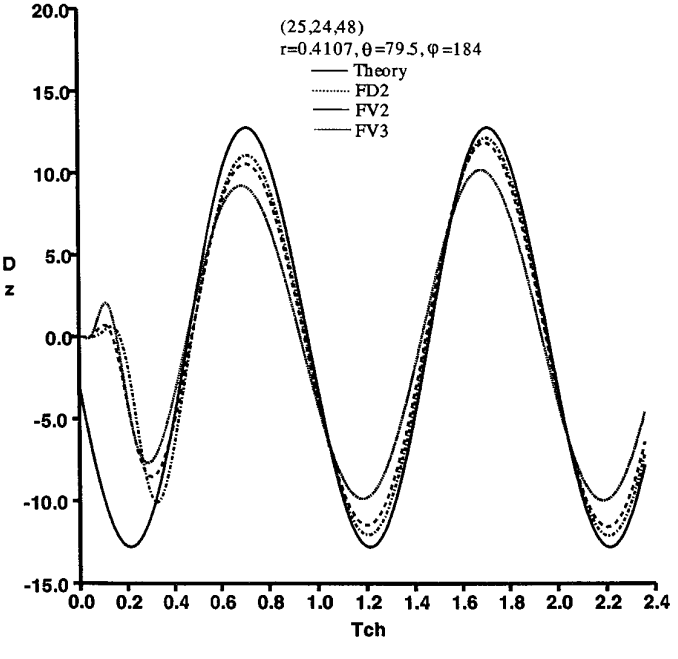

FIG. 8. Time trace of D_z, (25, 24, 48) grid.

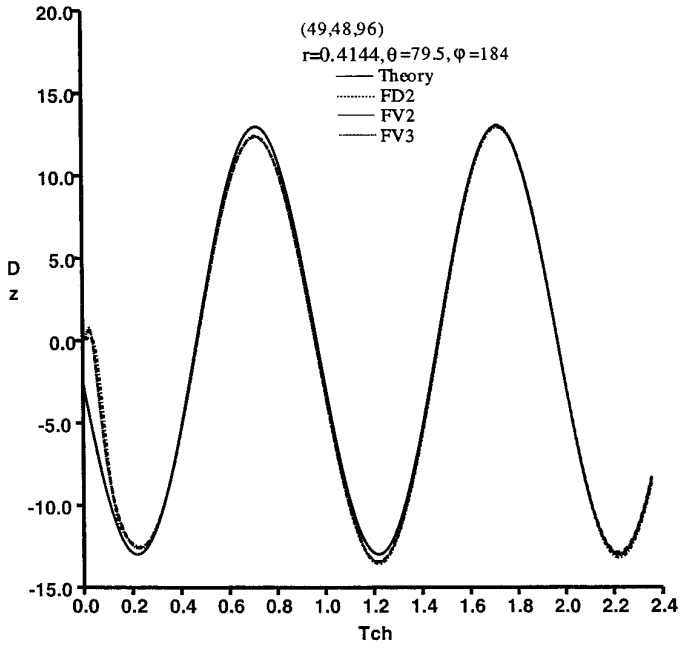

FIG. 9. Time trace of D_z, (49, 48, 96) grid.

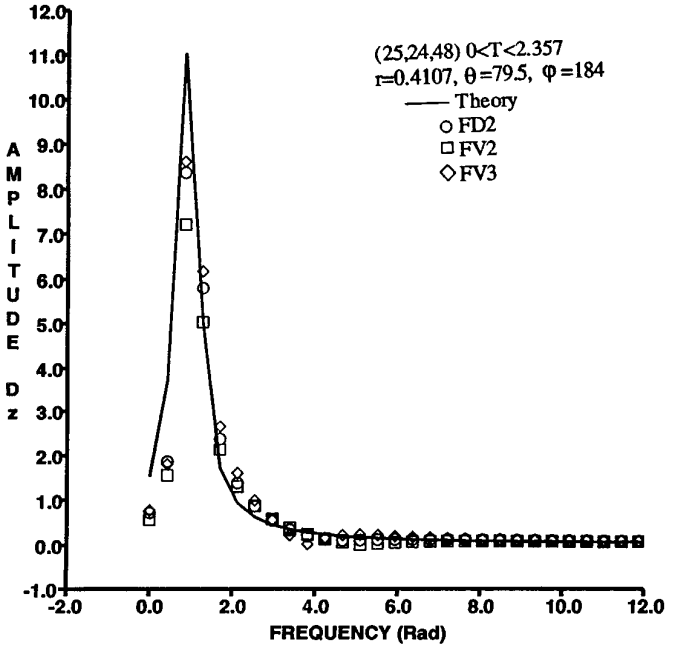

FIG. 10. Spectral analysis of D_z, (25, 24, 48) grid.

any point in the field. The analysis is too time consuming to apply to all computed dependent variables over the entire field. Therefore, the spectral analysis is only performed for a few randomly selected points from the three mesh systems. Since the mesh systems are not shared between the finite-difference and the finite-volume schemes and scaled to an unit sphere, data sampling at a common point among six grid systems is not attempted at present. Instead the point spectral analyses are conducted along the ray defined by $\theta = 79.5$, $\phi = 184$, and $0.4107 < r < 0.4144$. A two-hundred term Fourier series is used to perform the spectral analysis. The data sample includes the transient state to reflect the worst possible error and provides the longest period for high temporal resolution.

Figure 10 presents a comparison of the point spectral results on the (25, 24, 48) mesh system. The analysis is conducted for the z-component of electric intensity. The computed results compared with the theory exhibit a persistent leading phase error from the lowest frequency mode to higher harmonics. The relative phase errors of the FD2, FV2, and FV3 at the primary frequency are 1.0553, 1.1044, and 1.0465, respectively. The error in computed amplitude is exaggerated by including the overwhelming difference during the transient period (see Fig. 8), but it still reflects correctly the relative dissipative error of the three schemes investigated. On the coarsest grid system, numerical results by the second-order finite volume scheme contain higher dissipative and dispersive errors than the finite-difference counterpart. The numerical result generated by the FV3 scheme possesses the least dispersive and dissipative errors. The magnitude in under-predicted wave amplitude by the FV3 scheme is less than half to that of the FV2 procedure. The difference between results of FD2 and FV3 is 2.284%.

The point spectral analysis of the z-component electric intensity on the (37, 36, 72) mesh system is given in Fig. 11. On this mesh system, numerical results of the three

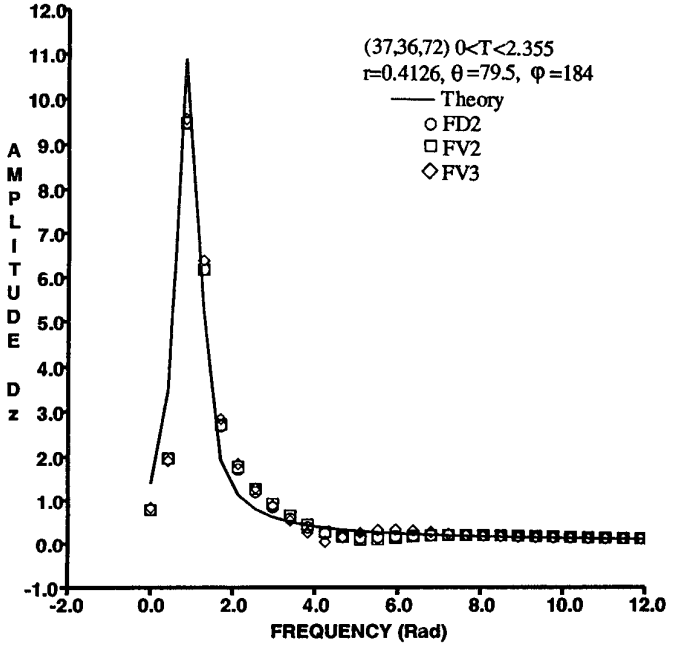

FIG. 11. Spectral analysis of D_z, (37, 36, 72) grid.

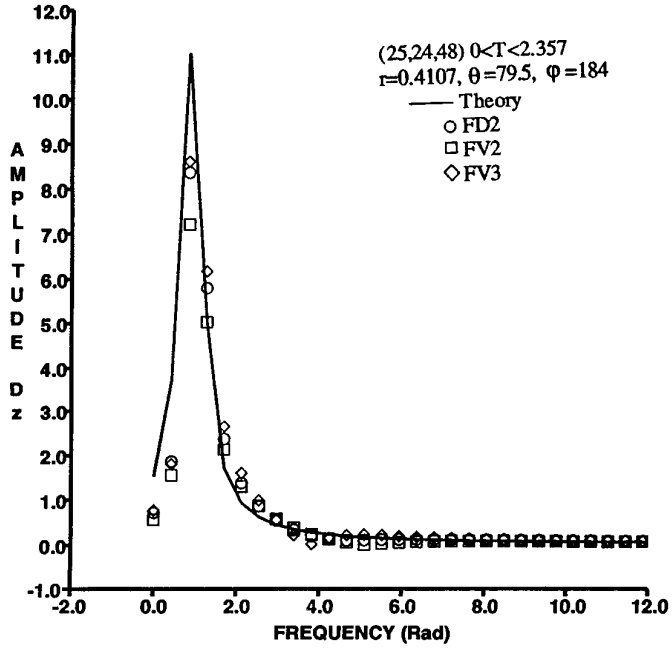

FIG. 12. Spectral analysis of D_z, (49, 48, 96) grid.

studied procedures are essentially identical. The relative phase errors associated with the FD2, FV2, and FV3 schemes are 1.0247, 1.0269, and 1.0247, respectively. The mesh distribution for these computations ensures that each wavelength is supported by 15 nodes. In this circumstance, the relative phase errors of FD2 and FV3 are identical. The difference in the primary wave amplitude predictions from FD2 and FV2 procedures is only 0.158%, favoring the finite-difference scheme. The third-order finite-volume scheme still produces the best agreement with the theoretical value in calculated amplitude of the dominant frequency.

Figure 12 depicts the comparison of results from the spectral analysis on the finest mesh system (49, 48, 96). Now all relative phase errors from three numerical procedures are reduced even more significantly. Both the second-order schemes FD2 and FV2 show a value of 1.0044, and the magnitude of the error for the third-order finite-volume scheme yields a surprisingly higher value of 1.0054. The higher value of dispersive error from the FV3 scheme may result from the inadequate implementation of the compatibility condition previously mentioned. This issue will be continuously pursued until improvement is obtained. Among the three numerical results, the calculated amplitudes at the principal frequency have a maximum difference of 0.3701%. Now the best result is generated by the second-order finite-volume scheme, which in part reflects its more rapid response to the perturbation in the transient period than that of the FV3 scheme. This particular behavior has been pointed out in the discussion of Figs. 8 and 9. In summary, all results from the point spectral analyses have substantiated fully the earlier observations made by studying the instantaneous values in space and the time trace of selected field variables.

IX. CONCLUSIONS

A three-dimensional finite-difference flux vector splitting procedure for solving the Maxwell equations in the time domain has been successfully developed. In particular a detailed eigenvector analysis is completed and verified for the Maxwell equations in a general curvilinear coordinate. This formulation can be used as the basic framework for future finite-difference flux splitting procedures. All characteristic-based methods both the finite-difference and finite-volume procedures produced excellent results when applied to an oscillating electric dipole problem. Within the limit of numerical error, the second-order characteristic-based methods with honor the physical zone of dependence, suppress completely the reflected wave from the truncated computational boundary.

On a highly stretched and non-rectangular quadrilateral mesh system, finite-volume schemes reveal degradations in numerical accuracy. The numerical error appears as a leading phase error. Once a sufficient number of cells have been provided to resolve wave motion (15 nodes per wavelength), the dissipative and dispersive error are substantially reduced. Two second-order windward finite-difference and finite-volume procedures generated solutions of comparable accuracy.

ACKNOWLEDGMENT

The authors appreciate computing support from the HPC Department of Defense shared resource center at CEWES, Vicksburg, Mississippi.

REFERENCES

1. A. Taflove, *Comput. Systems Engrg.* **3**(1–4), 153 (1992).
2. V. Shankar, *Research to Application Supercomputing Trends for the 90's: Opportunities for Interdisciplinary Computations,* AIAA Preprint 91-0002 (January, 1991).
3. D. A. Anderson, *Interdisciplinary Applications of Simulation CFD and Radar Cross-Section,* AFTAL-TR-88-1987, (Wright Laboratory, Eglin Air Force Base, June 1989).
4. J. S. Shang, *Characteristic Based Methods for the Time Domain Maxwell Equations,* AIAA Preprint AIAA-91-0606 (January 1991).
5. J. S. Shang, *A Fractional-Step Method for Solving 3-D Time-Domain Maxwell Equations,* AIAA Preprint 93-0461 (January 1993); also *J. Comput. Phys.* **118,** 109 (1995).
6. R. Higdon, *Math. Comput.* **47**(175), 437 (1986).
7. B. Enquist and A. Majda, *Math. Comput.* **31,** 629 (1977).
8. G. Muir, *IEEE Trans. Electromag. Comput.* **EMC-23**(4), 377 (1981).
9. R. Courant and D. Hilbert, *Mthods of Mathematical Physics, Vol. II, Partial Differential Equations* (Interscience, New York, 1965).

10. J. S. Shang and D. Gaitonde, *Characteristic-Based, Time-Dependent Maxwell Equations Solvers on a General Curvilinear Frame*, AIAA Preprint 93-3178, (July 1993), also *AIAA J.* **33**(3), 491 (1995).
11. P. Roe, *J. Comput. Phys.* **43,** 357 (1981).
12. B. Van Leer, *Flux-Vector Splitting for the Euler Equations*, TR 82-30 (ICASE, Sept. 1982).
13. J. L. Thomas and R. W. Walters, *AIAA J.* **25**(4) 527 (1987).
14. B. P. Leonard, *Int. J. Numer. Methods Fluids* **8,** 1291 (1988).
15. R. F. Warming and R. M. Beam, *Factored Schemes for Conservation Laws SIAM-AMS Proc.* **11,** 85 (1978).
16. J. A. Kong, *Electromagnetic Wave Theory* (Wiley, New York, 1986).
17. R. R. Harrington, *Time-Harmonic Electromagnetic Fields* (McGraw–Hill, New York, 1961).
18. E. C. Jordan, *Electromagnetic Waves and Radiating Systems* (Prentice–Hall, New Jersey, 1960).
19. J. L. Steger and R. F. Warming, *J. Comput. Phys.* **40,** 263 (1981).
20. K. A. Bagrinovskii and S. K. Godunov, *Dokl. Akad. Nauk USSR* **115,** 431 (1957).
21. N. Y. Yanenko, *Sibirsk. Math. Zh.* **5,** 1430 (1964).
22. B. Carnahan, H. A. Luther, and J. O. Wilkes, *Applied Numerical Methods* (Wiley, New York, 1969).
23. J. S. Shang, K. C. Hill, and D. A. Calahan, *Performance of a Characteristic-Based 3-D, Time-Domain Maxwell Equations Solver on a Massively Parallel Computer,* AIAA Paper 93-3179 (July 1993); also *Appl. Comp. Elec. Soc.* **10**(1), 52 (1995).
24. J. S. Shang, D. A. Calahan, and B. Vikstrom, *Performance of a Finite-Volume CEM Code on Multicomputers,* AIAA Paper 94-0236 (January 1994).
25. J. S. Shang and D. Gaitonde, *Scattered Electromagnetic Fields of a Reentry Vehicle,* AIAA Paper 94-0231 (January 1994), also *J. Spacecraft Rockets* **32**(2), 294 (1995).